1402 *Biochemistry* **1999,** *38,* 1402−1414

Solution Structure and Dynamics of the CX_3C Chemokine Domain of Fractalkine and Its Interaction with an N-Terminal Fragment of CX_3CR1[†,‡]

Laura S. Mizoue,[§] J. Fernando Bazan,[||] Eric C. Johnson,[§] and Tracy M. Handel*[,§]

Department of Molecular and Cell Biology, University of California at Berkeley, Berkeley, California, 94720, and Department of Molecular Biology, DNAX Research Institute, Palo Alto, California, 94304

Received August 25, 1998; Revised Manuscript Received November 17, 1998

ABSTRACT: Fractalkine, a novel CX_3C chemokine, is unusual because of both its membrane-associated structure and its direct role in cell adhesion. We have solved the solution structure of the chemokine domain of fractalkine (residues 1−76) by heteronuclear NMR methods. The 20 lowest energy structures in the ensemble have an average backbone rmsd of 0.43 Å, excluding the termini. In contrast to many other chemokines which form homodimers, fractalkine's chemokine module is monomeric. Comparison of the structure to CC and CXC chemokines reveals interesting differences which are likely to be relevant to receptor binding. These include a bulge formed by the CX_3C motif, the relative orientation of the N-terminus and 30's loop (residues 30−38), and the conformation of the N-loop (residues 9−19). ^{15}N backbone relaxation experiments indicate that these same regions of the protein are dynamic. We also titrated ^{15}N-labeled protein with a peptide from the N-terminus of the receptor CX_3CR1 and confirmed that this region of the receptor contacts the fractalkine chemokine domain. Interestingly, the binding site maps roughly to the regions of greatest flexibility and structural variability. Together, these data provide a first glimpse of how fractalkine interacts with its receptor and should help guide mutagenesis studies to further elucidate the molecular details of binding and signaling through CX_3CR1.

Surveillance of tissues for foreign pathogens involves the continuous recirculation of lymphocytes between blood, tissue, and lymph and the unidirectional recruitment of granulocytes and monocytes from blood to tissue in response to injury or infection (*1*, *2*). The current model for leukocyte migration involves several steps that are controlled at the molecular level by chemoattractant cytokines (chemokines) and adhesion molecules (*3*). First, leukocytes loosely tether themselves to the endothelium via the selectin family of carbohydrate-binding proteins (*4*). The binding is transient unless a signal is given to the cell that enables firm attachment to the endothelium mediated by integrin molecules (*5*). In the final step, diapedesis occurs, and the leukocyte moves through the tissue following a chemotactic gradient. Chemokines are implicated both in triggering leukocyte adhesion and in directing their migration through the extravascular space, but the mechanistic details of these processes are still poorly understood.

Chemokines have been characterized as small (8−12 kDa) secreted proteins that are divided into three classes (CXC, CC, and C) on the basis of the number and arrangement of N-terminal cysteine residues. In the CXC chemokines, the first two cysteines are separated by a single amino acid, while in the CC chemokines they are adjacent. The lone C chemokine, lymphotactin, lacks both the first and third cysteines that form a disulfide bridge in the other families (*6*). The classes tend to segregate functionally with different proteins causing chemotaxis of different leukocyte subpopulations. In general, CXC chemokines attract neutrophils, CC chemokines attract macrophages and T cell subpopulations, while lymphotactin attracts T and NK cells (*7*).

A fourth type of human chemokine was discovered recently that differs significantly from all other members of the superfamily. This protein, called fractalkine/neurotactin/NKAF, contains a novel CX_3C spacing of the cysteine motif and has a unique membrane-bound structure (*8*−*10*). The domain organization includes a 37-residue intracellular tail, a short membrane-spanning region, and an extended, mucin-like stalk which tethers the N-terminal chemokine domain to the cell surface. Its unusual architecture provides a means of retention under blood flow that differs from soluble chemokines which have patches of basic residues (the heparin-binding domain) that may promote immobilization by cell surface proteoglycans or extracellular matrix components (*11*).

Thus far, little is known about the function of fractalkine *in vivo*. Unlike most chemokines, fractalkine is not expressed in peripheral blood leukocytes (*8*, *9*) but is strongly expressed on the surface of endothelial cells where it can induce adhesion of T-cells, monocytes, and NK cells (*8*). High levels of fractalkine are also found in the brain, and its expression in microglia is rapidly upregulated in murine models of EAE,[1] suggesting that the protein may be important in brain inflammatory responses (*9*). Other biological roles besides

---

[†] This work was supported by grants awarded to T.M.H. from the National Institutes of Health, American Heart, and the PEW Scholars Program in Biomedical Science.

[‡] The coordinates have been deposited with the Brookhaven Protein Data Bank under the accession code 1B2T.

* To whom correspondence should be addressed. Phone: 510-643-9313. Fax: 510-643-9290. E-mail:handel@paradise1.berkeley.edu.

[§] University of California at Berkeley.

[||] DNAX Research Institute.

10.1021/bi9820614 CCC: $18.00

inflammation have also been postulated including developmental regulation of cells in the CNS (*9*), cellular communication between neurons and microglia, and regulation of neuronal plasticity in both normal and degenerated brain tissue (*12*).

Chemokines mediate their biological effects by binding and signaling through seven-transmembrane GPCRs. V28, an orphan GPCR, was identified recently as a receptor for fractalkine and designated CX_3CR1 (*13*). CX_3CR1 is expressed on leukocytes (*13*) and at high levels in the brain (*14*). In addition to its role as a signaling receptor, CX_3CR1 can function in *in vitro* assays as a cofactor for HIV entry into cells (*15*, *16*).

Adherence of CX_3CR1 transfected cells and NK cells to endothelial cells expressing membrane-bound fractalkine occurs in the absence of downstream activation of integrins or signaling via pertussis toxin sensitive G-proteins. This suggests that fractalkine acts directly in mediating cell−cell adhesion (*13*). Fractalkine also can be released from the membrane as a 95 kDa glycoprotein containing the chemokine module and a large portion of the mucin stalk (*8*). While the tethered form of the protein is necessary for inducing adhesion, the chemokine domain alone is sufficient for high-affinity receptor binding and activation (*8*, *13*).

To fully understand the molecular mechanisms by which fractalkine acts as a chemoattractant and adhesion molecule, one needs structural information on the ligand and ligand−receptor complex. Herein, we present the backbone dynamics and high-resolution solution structure of the chemokine module of fractalkine (residues 1−76). This represents the first structure determination of a CX_3C chemokine. We show that the fractalkine chemokine domain (FRCD) is monomeric, and we compare its structure to other CC and CXC chemokines. Our results show a number of distinct differences between FRCD and other chemokine family members, many of which are associated with the small variation in cysteine spacing. We also titrated FRCD with a peptide fragment of the N-terminal ectodomain of CX_3CR1 to begin to understand how it interacts with its receptor. Interestingly, the residues which appear to contact this portion of the receptor are localized to regions which are the most flexible and show the largest structural differences relative to other chemokines.

MATERIALS AND METHODS

Expression and Purification of FRCD. DNA encoding residues 1−76 of fractalkine was subcloned into the T7-driven expression vector pAED4 (*17*) and transformed into the *Escherichia coli* strain BL21/pLysS. Cells were grown at 37 °C in MOPS minimal media (*18*) containing ^{13}C-glucose (2 g/L) and/or ^{15}N-ammonium sulfate (1 g/L), 100 μg/mL of ampicillin, and 25 μg/mL chloramphenicol. When the cell density reached 0.7 OD_{600}, protein expression was induced by adding isopropyl β-D-thiogalactopyranoside (IPTG) to a final concentration of 0.5 mM. The protein was isolated from inclusion bodies as follows:

E. coli cell paste from a 1.5 L growth was sonicated in 150 mL of buffer (10 mM potassium phosphate, 5 mM EDTA, 1 mM phenylmethylsulfonyl fluoride, 5 mM benzamidine, pH 7.0) and centrifuged at 10000 rpm for 20 min. The cell pellet was washed twice with 50 mL of buffer containing detergent (25 mM potassium phosphate, 0.25% deoxycholate, pH 7.5) followed by two 50 mL washes in the same buffer without detergent. Refolding and oxidation of the two disulfides were achieved by solubilizing the pellet in a minimal amount of 6 M guanidinium chloride and diluting it 100-fold into a redox buffer containing 100 mM Tris, 5 mM EDTA, and 0.2 mM oxidized glutathione, 1 mM reduced glutathione, pH 8.0. After overnight stirring at 4 °C, the solution was adjusted to pH 7.0, centrifuged, filtered, and loaded onto a 30 mL Sepharose SP fast flow column. The column was washed with 2−3 bed volumes of 10 mM potassium phosphate, 5 mM EDTA, pH 7.0, and the protein was eluted with a salt gradient of 0.25−0.65 M in the same buffer. Final purification was achieved by reversed-phase HPLC on a Vydac C4 semi-prep column with a gradient of 26.0:73.9:0.1 to 38:61.9:0.1 acetonitrile/H_2O/trifluoroacetic acid, followed by lyophilization. Mass spectral analysis indicated that the protein was oxidized and the initiating methionine was retained. MH^+ (+Met): 8766.22 (calculated), 8766.37 (observed). The typical yield of purified protein was 7 mg/L.

Equilibrium Sedimentation. Analytical ultracentrifugation experiments were performed at 25 °C on a Beckman model XL-A ultracentrifuge. Protein samples were prepared in 100 mM sodium acetate, pH 5.0, and dialyzed overnight before dilution with the final dialysate to the desired concentrations. Loading concentrations ranged from 34 to 57 μM. Samples were centrifuged at 32000 and 40000 rpm, and equilibrium was assumed if no change in distribution was observed after 2 h intervals. Absorbance was measured at 280 nm, and the data were collected as an average of five successive radial scans using a 0.001 cm step size. The molecular weight M was obtained by fitting the data to the following equation:

$$A_r = A_0 \exp[MH(r^2 - r_0^{\,2}) + E]$$

where

$$H = (1 - \nabla\rho)\,\frac{\omega^2}{2RT}$$

In these equations, A_r is the absorbance at radius r, A_0 is the absorbance at the reference radius r_0, ∇ is the partial specific volume, ρ is the solvent density, ω is the angular velocity of the rotor, and E is a baseline offset. Partial specific volumes were calculated from the weight average of the partial specific volumes for individual amino acids. Data were fit to the equation by nonlinear least squares using the Microcal Origin software provided by Beckman for the XL-A. The quality of the fit was characterized by χ^2, the sum of

---

[1] Abbreviations: CCR, CC chemokine receptor; CXCR, CXC chemokine receptor; CNS, central nervous system; CT, constant time; DARC, Duffy antigen/receptor for chemokines; EAE, experimental autoimmune encephalomyelitis; GPCR, G-protein coupled receptor; HMQC, heteronuclear multiple-quantum coherence experiment; HSQC, heteronuclear single-quantum coherence experiment; IL-8, interleukin-8; MCP-1, monocyte chemoattractant protein-1; MCP-1P8A, MCP-1 with a point mutation of P8A; MGSA/GRO, melanoma growth stimulatory activity; MIP-1β, macrophage inflammatory protein-1β; NOE, nuclear Overhauser effect; R1, longitudinal relaxation rate; R2, transverse relaxation rate; RANTES, regulated upon activation, normal T-cell expressed and secreted; rmsd, root-mean-square deviation; SA, simulated annealing; SDF-1, stromal derived factor-1; TPPI, time-proportional phase incrementation; WT, wild type.

the squares of the residuals, and examination of the residuals for systematic deviation.

Heparin Binding. The heparin-binding affinity of FRCD was determined using a Biorad Econosystem equipped with a gradient monitor. Protein was loaded onto a 5 mL heparin column (Biorad Econopac) in 10 mM potassium phosphate, pH 7.5, and eluted with a 40 mL linear gradient of 0.1−1.0 M NaCl in the same buffer at a flow rate of 2.0 mL/min. Protein elution was monitored by absorbance at 280 nm. FRCD eluted at 0.22 M NaCl compared to 0.55 M NaCl for WT MCP-1 and 0.48 M NaCl for MCP-1P8A, a monomeric variant of MCP-1 (Paavola and Handel, unpublished results).

NMR Spectroscopy. NMR samples (∼1.6 mM) were prepared by dissolving lyophilized protein in 90% H_2O/10% D_2O, 5 mM EDTA-d_{12}, 0.05% sodium azide and adjusting the pH to 5.0 by adding NaOH. All NMR experiments were carried out under identical conditions on a 600 MHz Bruker DMX spectrometer equipped with four channels and a single-axis *z*-gradient probe. The temperature (meter reading= 25 °C, actual temperature = 22.5 °C) was calibrated with sodium 3-trimethylsilylpropionate (TSP). Chemical shifts were referenced at 25 °C according to the method of Wishart and co-workers (*19*).

The pulse sequences cited below were modified to include pulsed-field gradients for artifact and solvent suppression. Quadrature detection in the indirect dimensions was achieved by STATES-TPPI except for certain ^{13}C dimensions where STATES was used to place axials in the center rather than at the edge of the spectrum. The ^{1}H spectral width in the directly detected dimension was 8090.615 Hz, and the ^{15}N spectral width was 700.0 Hz for all experiments. Complete details of the data collection are available as supporting material or by e-mail from the corresponding author.

Sequential assignments for backbone ^{15}N, $^{1}H_N$, $^{13}C_\alpha$, and side chain $^{13}C_\beta$ nuclei were obtained from 3D HNCACB (*20*) and CBCA(CO)NNH (*21*) experiments acquired on a uniformly labeled $^{15}N/^{13}C$ sample in 90% H_2O/10% D_2O. ^{13}C and ^{1}H side chain assignments were obtained from a 4D HCC(CO)NNH experiment (*22*). Because this experiment has limited digital resolution, a 3D HCCH-TOCSY (*23*) was also collected to increase the precision of the side chain chemical shifts. Aromatic side chain assignments were obtained from an aromatic version of the CT ^{13}C−HSQC (*24*) together with a relayed version of the experiment (*25*).

NOESY experiments included a 3D ^{15}N-separated NOESY−HSQC (*26*), a 3D ^{13}C-separated NOESY−HSQC (*27*), and a 4D $^{13}C/^{13}C$-separated HMQC−NOESY−HSQC (*28*, *29*) all collected on a uniformly labeled $^{15}N/^{13}C$ sample in 90% H_2O/10% D_2O using 150 ms mixing times.

$^{3}J_{NH\alpha}$ coupling constants were measured using a 3D HNHA experiment (*30*) to provide backbone ϕ angle restraints. $^{3}J_{C\gamma N}$ and $^{3}J_{C\gamma C'}$ were measured using *J*-modulated versions of a 2D CT ^{13}C−HSQC (*31*, *32*) to provide stereospecific assignments for Val residues and χ_1 restraints for Val, Thr, and Ile residues. 3D HNHB (*33*) and 3D HACAHB (*34*) experiments were used to obtain stereospecific assignments and angular restraints for H_β methylene groups. Long-range ^{13}C-^{13}C couplings were measured using the $^{3}J_{CC}$ experiment (*35*) to obtain χ_2 restraints for Leu and Ile residues.

Slowly exchanging amides were identified by recording a series of 2D ^{1}H-^{15}N HSQC experiments (*36*) immediately following dissolution of lyophilized protein in D_2O.

Data Processing and Structure Calculations. All NMR spectra were processed on a Silicon Graphics R4400 Indigo2 workstation using the program AZARA (Wayne Boucher, unpublished results). Deconvolution of time domain data was used to remove residual solvent signal (*37*). In the directly detected dimension, the data were zero-filled, windowed with a 75° phase-shifted squared sinebell, and Fourier transformed (FT). For 3D experiments, the indirectly detected dimensions were processed using a 2D maximum entropy algorithm. The 4D $^{13}C/^{13}C$-separated NOESY was processed in a similar manner using 2D maximum entropy followed by conventional FT of the third indirect dimension. The 4D HCC(CO)-NNH experiment was processed using a 3D maximum entropy algorithm.

Spectra were analyzed within the graphics program ANSIG3.3 (*38*). Structure calculations were done on Silicon Graphics R-4400 computers with the program X-PLOR (*39*). Calculations were performed with restrained molecular dynamics-simulated annealing procedures coupled with the Ambiguous Restraints for Iterative Assignment (ARIA) extension of Nilges (*40*, *41*) and with floating plus active swapping of stereospecific assignments (*42*). A more complete description of the structure calculations is provided in the results section.

Titration of FRCD with a Peptide from the N-terminus of the Receptor CX_3CR1. A peptide corresponding to residues 2−19 of the N-terminus of CX_3CR1 was chosen by analogy to a peptide fragment of the chemokine receptor CCR2B that binds to the CC chemokine MCP-1 (Mizoue and Handel, unpublished results). This peptide (QFPESVTENNFEYDDLAEA) was synthesized on an ABI 431A synthesizer and purified by reversed-phase HPLC. 2D ^{1}H-^{15}N HSQC spectra were recorded on a 0.25 mM sample of ^{15}N-labeled FRCD (90% H_2O/10% D_2O, pH 5.0) containing various concentrations of peptide up to a peptide/FRCD ratio of 5:1. The spectra were collected at 22.5 °C with 256 (t1) × 1024 (t2) real points corresponding to acquisition times of 182 ms (t1) and 63 ms (t2).

Dynamics. Backbone dynamics experiments were recorded on uniformly labeled ^{15}N samples in 90% H_2O/10% D_2O using versions of published pulse sequences (*43*) modified to include gradients and waterflip back pulses (*36*, *44*). The data were collected on a 1.6 mM sample (data not shown) and on a more dilute 0.5 mM sample to evaluate potential effects of nonspecific aggregation. Spectra were acquired with 128 (t1) × 1024 (t2) real points corresponding to acquisition times of 91 ms (t1) and 63 ms (t2). R1 experiments were recorded with delays of 0.010, 0.061, 0.112 (two experiments), 0.194, 0.265, 0.408, 0.541, 0.806, and 1.061 s. R2 experiments were recorded with delays of 0.008, 0.016, 0.024, 0.040, 0.056 (2 experiments), 0.080, 0.104, 0.136, and 0.176 s. All data sets were processed in AZARA using a conventional FT, and fitted peak heights were measured using the program PRIISM (*45*). R1 and R2 values were obtained by fitting the cross-peak intensities to a decaying exponential. Uncertainties in the relaxation rates were taken as the standard deviation of the curve fit. NOE values were obtained from the ratio of peak intensities recorded with and without proton saturation. Uncertainties in the NOE values were obtained by propagating the uncertainties in peak heights which were taken to be the

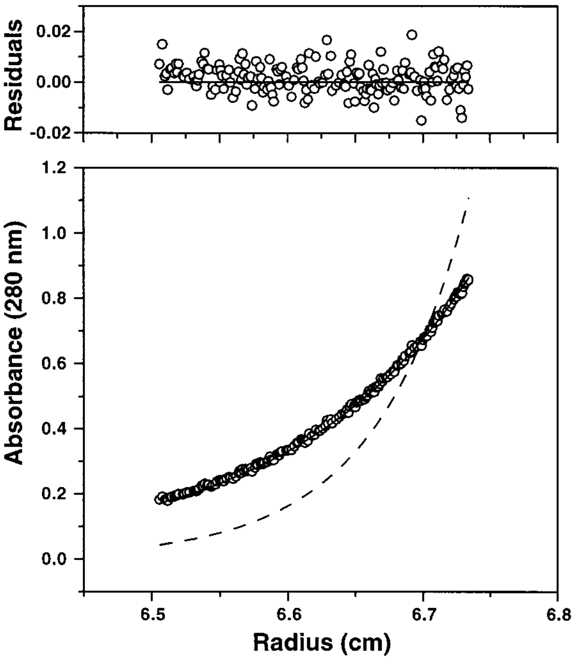

FIGURE 1: Sedimentation equilibrium profile for FRCD. The filled and dashed lines are the theoretical curves for monomer and dimer, respectively.

baseplane noise in the spectra. The recycle delay was 2.0 s for the R1 and R2 experiments and 6.0 s for the NOE experments. Order parameters and correlation times were determined from these data using the program DYNAMICS (*46*).

RESULTS

FRCD is Monomeric. Most chemokines oligomerize to an extent that depends heavily on solution conditions. Above micromolar concentrations, many form homodimers as indicated by the majority of dimeric structures that have been solved (47−51), while at nanomolar concentrations, the monomeric form predominates. In the case of FRCD, analytical ultracentrifugation indicates that, at least up to 57 μM, the protein exists as a monomeric species in solution at pH 5.0. Representative sedimentation equilibrium data are shown in Figure 1. The curve fit to the equilibrium distribution shows a random scattering of the residuals and matches a theoretical curve calculated for a 8.8 kDa monomer.

Gel filtration and pulsed field gradient diffusion experiments were also conducted to determine whether the protein remains monomeric at higher concentrations. At concentrations up to 700 μM, FRCD eluted as a single, symmetric peak from a BioSil SEC125 column equilibrated in 25 mM sodium acetate, 150 mM NaCl, pH 5.0 (data not shown). Furthermore, its retention time was similar to that of MCP-1P8A, an 8.8 kDa monomeric mutant of MCP-1 (*52*). It was also identical to that of ubiquitin (8.7 kDa monomer), whereas WT MCP-1 (17.6 kDa dimer) eluted earlier (data not shown). However, pulsed field gradient diffusion experiments (*53*) conducted under the actual NMR conditions (~1.6 mM protein in 90% H_2O/10% D_2O, pH 5.0) indicated that FRCD had a self-diffusion coefficient (1.04 × 10^{-6} cm^2/s) between that of MCP-1P8A (1.149 × 10^{-6} cm^2/s) and WT MCP-1 (0.841 × 10^{-6} cm^2/s). This discrepancy may be due to different salt concentrations used in the various experiments or nonspecific aggregation of the protein at the higher concentration. We suspect the latter reason since the correlation time of the protein calculated from ^{15}N relaxation experiments (see below) was larger at high protein concentration (τ_m = 6.7 ns at 1.6 mM vs 6.0 ns at 0.5 mM). As we failed to observe NOEs that were consistent with a dimer interface or concentration-dependent changes in chemical shifts, it does not appear that the protein is oligomerizing to any significant extent.

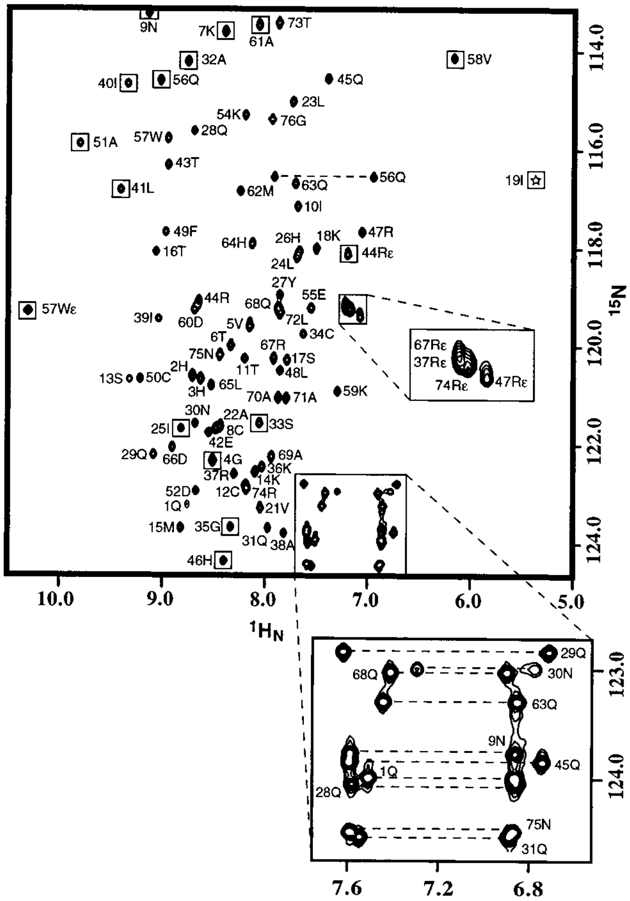

FIGURE 2: ^1H-^{15}N HSQC spectrum of FRCD. Aliased cross-peaks are identified with boxes. Asn and Gln NH_2 and Arg HN_ϵ cross-peaks are shown as enlargements. The Ile19 cross-peak, indicated here by a star, is visible at lower contour levels.

Chemical Shift Assignments and Restraints. The ^1H-^{15}N HSQC of FRCD is shown in Figure 2. The spectral dispersion is excellent, and all amide backbone resonances are visible with the exception of Met0. Consequently, assignment of backbone and side chain ^1H, ^{15}N, and ^{13}C resonances, with the exception of the epsilon carbons of the five histidines and all carbonyl carbons, was accomplished in a straightforward manner using ANSIG procedures similar to those previously described (*51*). A table of the chemical shift assignments is available as Supporting Information or by e-mail from the corresponding author.

NOE distance restraints were derived from the 3D ^{15}N-separated NOESY, 3D ^{13}C-separated NOESY, and 4D ^{13}C/^{13}C-separated NOESY experiments. The spectra were peak-picked either manually or using automated AZARA routines launched from within ANSIG. Cross-peaks were integrated by box summation, and the NOE intensities were classified as strong (0−2.7 Å), medium (0−3.3 Å), weak (0−5.0 Å), and very weak (0−6.0 Å). Pseudoatom corrections were not applied to unassigned stereocenters (see below). The peak-picked, integrated cross-peak tables were then output from ANSIG and automatically converted into distance restraint tables using the "connect" utility in AZARA (Wayne Boucher, unpublished results). This program matches the chemical shift of each NOE cross-peak with all assignment possibilities within a given tolerance on the basis of the chemical shift database described in the previous paragraph and outputs a restraint file in X-PLOR format. The number and distribution of NOEs are described in the next section.

Forty four backbone ϕ angle restraints were obtained from measurements of ${}^3J_{\mathrm{NH}\alpha}$. Small J values (<5 Hz) indicative of α-helices were assigned ϕ values of $-60 \pm 30°$. Large J values (>8 Hz) indicative of β-sheet structure were assigned ϕ values of $-120 \pm 30°$. Residues with indeterminate ϕ angles were constrained to $-90 \pm 90°$ if the intraresidue $\mathrm{H_N H_\alpha}$ NOE was weaker than the interresidue NOE (*54*). ${}^3J_{\alpha\beta}$ values from the 3D HACAHB experiment were used together with qualitative estimates of ${}^3J_{\mathrm{NH}\beta}$ from the 3D HNHB to stereospecifically assign β methylene protons and to obtain χ_1 torsion angle restraints. Stereospecific assignments for Pro H_β's were determined based on the intensities of $\mathrm{H_\alpha H_\beta}$ NOEs. For Ile, Val, and Thr residues, χ_1 torsion angle restraints were obtained from measurement of ${}^3J_{\mathrm{C}\gamma\mathrm{N}}$ and ${}^3J_{\mathrm{C}\gamma\mathrm{C}'}$; these experiments also allowed stereospecific assignment of one of the Val residues. Leu and Ile χ_2 torsion angles were determined from ${}^3J_{\mathrm{CC}}$ measurements obtained from a long-range ^{13}C-^{13}C correlation experiment. Stereospecific assignments of Gln and Asn $\mathrm{NH_2}$ protons were based on the relative intensities of intraresidue NOEs to side chain methylene protons. By using these methods, we were able to stereospecifically assign 19 of the 41 nondegenerate β methylene groups (11 were degenerate), 5 of the 9 nondegenerate methyl groups (none were degenerate), and 5 of 11 $\mathrm{NH_2}$ proton pairs. A total of 34 χ angles were determined and restricted to ±30° around the canonical values for g+, g-, and t. In cases where stereospecific assignment was not possible, the individual resonances of the methylene (or isopropyl groups) were assigned using an arbitrary but consistent convention in ANSIG and then treated with a floating plus swapping assignment procedure (see below) during the structure calculations.

Thirty hydrogen bond restraints were added in later stages of the refinement on the basis of evidence of slowly exchanging amide protons and secondary structure. Potential hydrogen bond acceptors were inferred by inspecting structures in INSIGHT (Biosym, San Diego CA); 4 hydrogen bonds had 2 or 3 possible acceptors and were treated as ambiguous (see below). The HN-acceptor distance was restrained between 1.7 and 2.2 Å, and the N-acceptor distance was restrained between 2.7 and 3.2 Å.

Structure Calculations. NMR structure calculations are typically performed in an iterative fashion after manual assignment of NOE data. In the first round of calculations, only those NOEs that have been unambiguously assigned to a single pair of protons are used to generate preliminary structures. Once the global fold of the protein is known, distance filtration is used to assign additional NOEs which are then included in the next round of calculations, and the process continues until no further assignments are possible. Not only is this strategy extremely time-consuming, but also it uses only a fraction of the available data in the initial calculations. Thus, depending upon the number, nature, and distribution of NOEs that are used in the initial calculations, bias may be introduced in the preliminary structures which can then be propagated in subsequent rounds. We chose a different approach based on a strategy developed by Nilges which allows inclusion of ambiguously assigned NOEs in the calculations (*40*, *41*). This is done by treating the NOEs as a $(1/r^6)^{-1/6}$ sum of all of the assignment possibilities. In principle, this method allows all NOE restraints, ambiguous and unambiguous, to be included at the outset, and therefore should provide the least biased approach toward structure determination. However, it does require a complete set of robust resonance assignments and a sufficient number of unambiguous NOEs to define the global fold of the protein. For the latter reason, we include 4D NOESY data, even for small proteins such as FRCD.

Our implementation of the method involved first outputting NOE restraint tables as described in the preceding section. Starting conformations were then generated as random atomic coordinates within a 20 Å cube. Calculations were performed with the restrained molecular dynamics-simulated annealing procedure essentially as described by Nilges (*40*−*42*), using r^{-6} summing of NOEs including those involving equivalent protons in methyl groups, unresolved methylenes, and aromatic rings. All NOEs, ambiguous and unambiguous, were included at the outset. Angular restraints were also included. To avoid applying pseudoatom distance corrections, we treated unassigned stereocenters with floating chirality (*42*). Throughout the structure calculations, improper force constants that define the chirality of prochiral centers were set to 0, allowing the atoms to "float" into the proper configuration if defined by the NOE data. During the cooling stages of refinement, methylene protons or ispopropyl groups were also actively swapped since it has been shown that this gives superior results to floating or swapping alone (*42*). One difference in our implementation of active swapping compared to that described by Nilges is the acceptance criterion for swapped stereospecific assignments. In his approach, the swapped conformation is accepted if it gives rise to a lower NOE energy; otherwise the original conformation is restored. In our approach, the new conformation was accepted or rejected on the basis of a Metropolis criterion (Andrew Raine and Brian Smith, unpublished results) (*55*). In addition, methyl groups were swapped at earlier stages of the refinement, independently of methylene groups, since the stereochemistry of the methyl groups should have a larger impact on the structure. The temperature used in the Metropolis criterion was optimized separately for methyl versus methylene groups on the basis of the rate and extent of convergence of conformations within the ensemble of structures.

In successive rounds of calculations, structure refinement and iterative NOE assignment were accomplished using Nilges' ARIA methodology. Typically, 30−40 structures were generated, and the 20−30 structures with the lowest energies were analyzed for restraint violations. Restraints that were systematically violated were excluded from the next round of structure calculations. It is important to note that, when NOE violations occurred, the data were examined in ANSIG to determine the cause. In the preliminary rounds of calculations, this identified a number of spurious peaks which were removed subsequently from the cross-peak list.

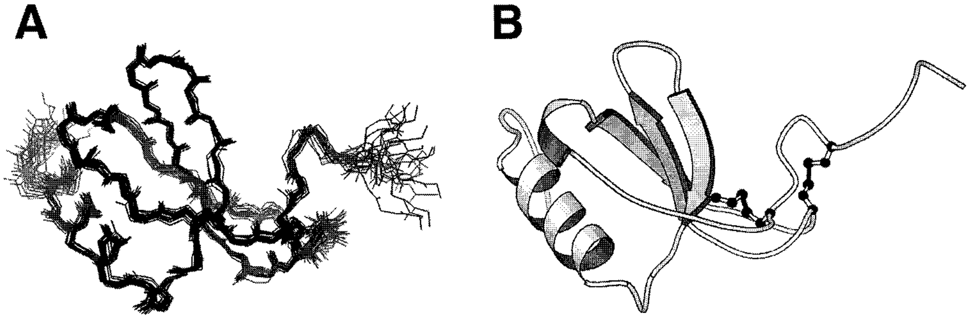

FIGURE 3: (A) Superposition of the 20 lowest energy structures of FRCD. Residues 1−4 and 71−76 are excluded. (B) A MOLSCRIPT diagram of the FRCD structure residues 1−76. The disulfides are shown as ball-and-stick representations.

The other common source of restraint violations stemmed from resonance overlap which resulted in an incorrect estimation of the peak volume. As the calculations proceeded, the number of ambiguous restraints was reduced gradually by removing assignment possibilities on the basis of distance filtration and percent contribution to the NOE intensity. The procedure was continued in subsequent rounds until the structures did not change significantly. In the last few rounds of calculations, H-bond restraints were included, 4 of which were treated ambiguously in a manner similar to that of the NOEs. In addition, duplicate restraints within each NOESY data set were removed with ARIA scripts such that only the shortest restraint was kept. At the beginning of the structure calculations, there were 2477 unambiguous cross-peaks. Of these, there were 1221 intraresidue, 257 sequential, 183 medium-range ($|i - j| \leq 4$), and 816 long-range ($|i - j| > 4$) NOEs. Cross-peaks (2313) had multiple assignment possibilities and an average level of ambiguity of 11, 12, and 4 in the 3D ^{15}N-separated NOESY, 3D ^{13}C-separated NOESY, and 4D ^{13}C/^{13}C-separated NOESY experiments, respectively. After the last round of calculations, the number of unambiguous cross-peaks increased to 3439 (1274 intraresidue, 601 sequential, 351 medium-range, and 1213 long-range NOEs), and the number of ambiguous cross-peaks was reduced to 491. The high number of unambiguous cross-peaks is due in large part to the redundancy between the 3D ^{13}C-separated and 4D ^{13}C/^{13}C-separated NOESY data sets.

Description of the Structures. Figure 3 shows the 20 lowest energy structures out of 70 for the final round of calculations together with a MOLSCRIPT (*56*) ribbon representation. Structural statistics for the ensemble are given in Table 1. The structures had no NOE distance violations greater than 0.3 Å and no torsion angle violations greater than 3°. The sequence plots of the rmsd from the minimized mean structure and the angular order parameters for ϕ, ψ, and χ_1 (Figure 4) show that the structure is well-defined except for the termini and the loop connecting β1 and β2. The average rmsd to the mean coordinates over residues 8−66 is 0.43 Å for backbone (N, C$_\alpha$, C) and 0.89 Å for all heavy atoms. A stereochemical analysis of the ensemble using PROCHECK (*57*) showed that, for residues 8−66, 78.4% of the residues were in the most favored region of the Ramachandran plot, 20.0% were in the allowed regions, 1.2% were in the generously allowed regions, and 0.4% were in the disallowed regions. Those in the generously allowed or disallowed classes correspond to residues in regions of high rmsd and mobility.

Table 1: Energy Statistics for an Ensemble of 20 Structures and Atomic rmsd to the Mean Structure

	energy (kcal·mol^{-1})	rmsd to target
NOE[a]	6.5 ± 0.7	0.0081 ± 0.0005 Å
dihedral angles[a]	0.33 ± 0.07	0.26 ± 0.03°
bonds	1.2 ± 0.1	0.00097 ± 0.00005 Å
angles	28.4 ± 0.6	0.288 ± 0.003°
van der Waals[b]	2.4 ± 0.5	
Lennard-Jones[c]	−208 ± 14	
	atomic rms deviations (residues 8−66)	
backbone	0.43 ± 0.09 Å	
heavy atom	0.89 ± 0.07 Å	

[a] The NOE and torsion angle terms were calculated with force constants of 25 kcal·mol^{-1}·Å^{-2} and 200 kcal·mol^{-1}·rad^{-2}, respectively. [b] The value of the quadratic van der Waals repulsion term was calculated with a force constant of 4 kcal·mol^{-1}·Å^{-4}. [c] The Lennard-Jones van der Waals energy was not included in the target function during simulated annealing.

Qualitatively, FRCD has a typical chemokine topology: the N-terminus (residues 1−7) is disordered up to the first cysteine (Cys8). Following the second cysteine (Cys12) is a long irregular loop (the N-loop, residues 9−19) which ends in a single turn of 3$_{10}$ helix (residues 20−23), conserved in all known chemokine structures. The 3$_{10}$ helix is followed by a 3-stranded antiparallel β-sheet (β1, residues 24−29; β2, residues 39−43; β3, residues 48−51) and a C-terminal helix (residues 56−67) which packs against the β-sheet. The C-terminus (residues 68−76) is disordered. Between β1 and β2 is a fairly long loop (the 30's loop, residues 30−38) which is in close proximity to the N-terminus by virtue of a disulfide bond between Cys8 and Cys34. The connection between β2 and β3 is a much shorter type I 3:5 turn with a G1 β-bulge, while a type I reverse turn connects β3 to the C-terminal helix. As in other chemokines, the second disulfide between Cys12 and Cys50 is left-handed. The chirality of the first disulfide, however, is not well-defined. This is in contrast to CC chemokines where it is left-handed and CXC chemokines where it is right-handed. Another unique feature of FRCD is the large bulge formed by the CX$_3$C motif (Figure 5).

Backbone Dynamics. ^{15}N relaxation experiments were conducted to probe the internal mobility of the protein backbone and to compare dynamic regions of the protein with those thought to be involved in receptor binding. Data were obtained for all residues with the exception of Met0, Gln1, and Ile19 (whose cross-peaks were too weak to measure accurately) and Cys12 and Arg74 (whose cross-peaks were overlapped). The experiments were recorded on 1.6 and 0.5 mM samples in order to evaluate the effects of possible nonspecific aggregation. With the exception of

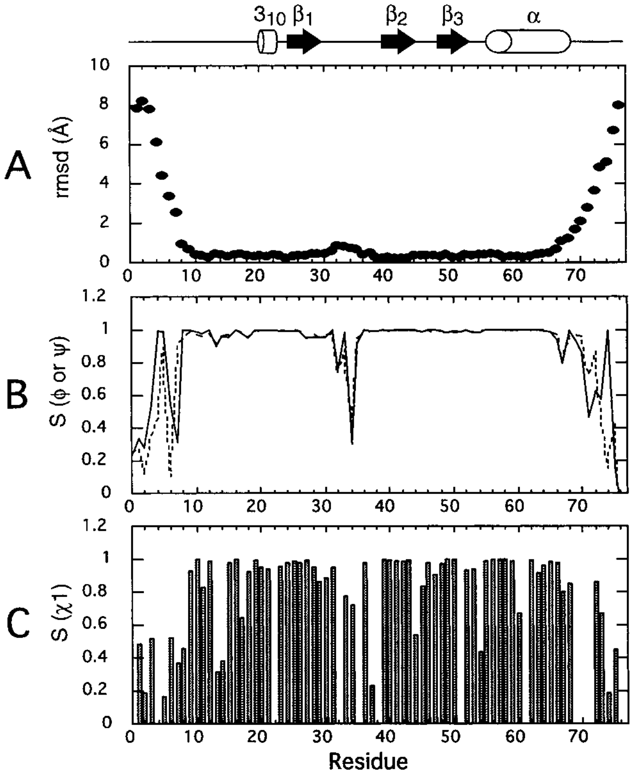

FIGURE 4: (A) Deviation of C_α rmsd from the mean of the ensemble. (B) Backbone angular order parameters: ϕ (continuous) and ψ (broken). (C) Side chain χ_1 angular order parameters. The secondary structure of the protein is shown above the figures.

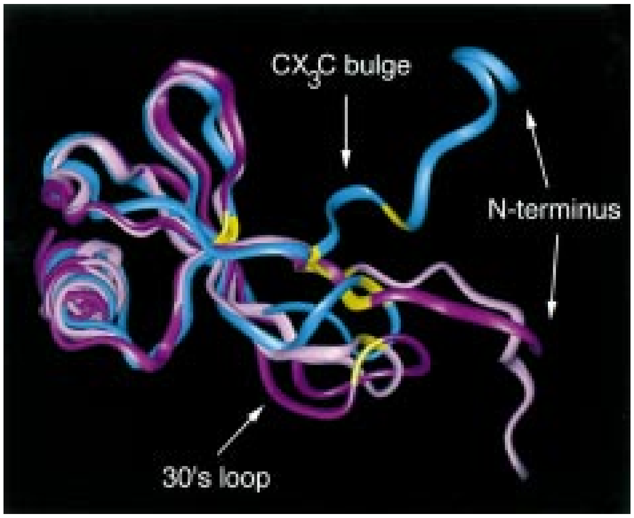

FIGURE 5: Superposition of FRCD (blue) with the monomers of the CC chemokine MCP-1 (pink) and the CXC chemokine IL-8 (purple). The positions of the cysteines are indicated in yellow. While the C-terminal helix and β-sheet superimpose quite well, there are large differences in the orientation of the N-termini and the 30's loops. This is further illustrated by comparison of the backbone rmsds to the difference in C_α positions of the first Cys between various chemokines superimposed onto FRCD. For MCP-1, these numbers are 1.35 and 6.17 Å; for IL-8, they are 1.49 and 8.14 Å. For GRO, MIP1-β, and RANTES the backbone rmsds are 1.51, 1.25, and 1.25 Å; the difference in the C_α position of the first Cys is 8.29, 7.45, and 5.84 Å, respectively. Least squares superposition was done over the following residues: FRCD residues 13−30 and 38−66; MCP-1 residues 13−16, 18−31, and 40−68; IL-8 residues 10−13, 15−28, and 38−66; GRO residues 12−29 and 39−67; MIP-1β residues 13−16, 18−31, and 39−67; and RANTES residues 12−15, 17−30, and 38−66.

differences in the overall correlation time (see above), both samples gave the same qualitative results.

Modelfree analysis of the relaxation data was done with the MATLAB program DYNAMICS (*46*). Using this method, the R1, R2, and NOE data were fit to five different dynamical models, and the appropriate model was chosen for each residue by evaluating the quality of the fit. The global correlation time (τ_m) was determined by conducting the model selection at fixed values of τ_m ranging from 5 to 7.0 ns. At τ_m values below 6.0 ns, there was a noticeable increase in the number of residues that required chemical exchange terms to fit the data. At τ_m values higher than 6.0 ns, there was an increase in both the number of residues that did not fit to any of the models and the number that required the two time scale model to adequately fit the data. Similar results were obtained when the optimization was performed only on "core" residues having T1/T2 values within one standard deviation of the mean and NOE ratios >0.65. Therefore, the optimal τ_m was taken to be 6.0 ns which is within the error estimate of the value calculated from T1/T2 values (*58*). Using this correlation time, only Val58 was not fit adequately; the data for this residue were fit to the simplest model where S^2 is the only parameter used to describe internal motion.

In these calculations, isotropic tumbling was assumed. Recent studies have shown that this can lead to erroneous interpretation of dynamics data because even small degrees of anisotropy can be misinterpreted as conformational exchange (*59*, *60*). However, when we included anisotropic rotational diffusion in our calculations, we did not see an improvement in the fit as measured by χ^2/df, the sum of the squares of the residuals per degree of freedom, nor did we see any significant changes in the number or identity of residues that the isotropic model had identified as undergoing slow internal motions.

The generalized order parameters (S^2), chemical exchange terms (R_{ex}), and local correlation times (τ_e) as a function of amino acid sequence are shown in Figure 6. Generalized order parameters provide a measure of the amplitude of internal motions, where $S^2 = 1$ means that a given N−H bond vector is rigid while $S^2 = 0$ indicates that the motion is unrestricted. Residues N-terminal to Cys8 and C-terminal to Ala69 exhibit low order parameters ($S^2 < 0.65$) due to rapid internal motions (τ_e) on the subnanosecond to nanosecond time scale. Both termini are poorly defined in the NMR structure (Figure 4A), and these data confirm that the disorder is caused by inherent mobility and not merely by a lack of experimental restraints. Excluding the termini, the average S^2 value over residues 8−69 is 0.85 ± 0.07. The order parameter for Cys8 falls below one standard deviation from the mean ($S^2 = 0.72$) and may explain why the chirality of the Cys8-Cys34 disulfide is poorly defined in the ensemble of structures. Other residues that exhibit low order parameters and subnanosecond fluctuations are clustered in loop regions and include Lys14, Met15 (N-loop), Cys34, Ala38 (30's loop), and Arg47 (3:5 turn connecting β2 and β3). Lys14 has the lowest order parameter ($S^2 = 0.65$) of all of the residues excluding the termini. It is interesting to note that the cross-peak of the preceding residue, Ser13, is severely line-broadened in the ^{15}N HSQC, which suggests that it undergoes slow conformational exchange on the millisecond to microsecond time scale. Slow conformational exchange

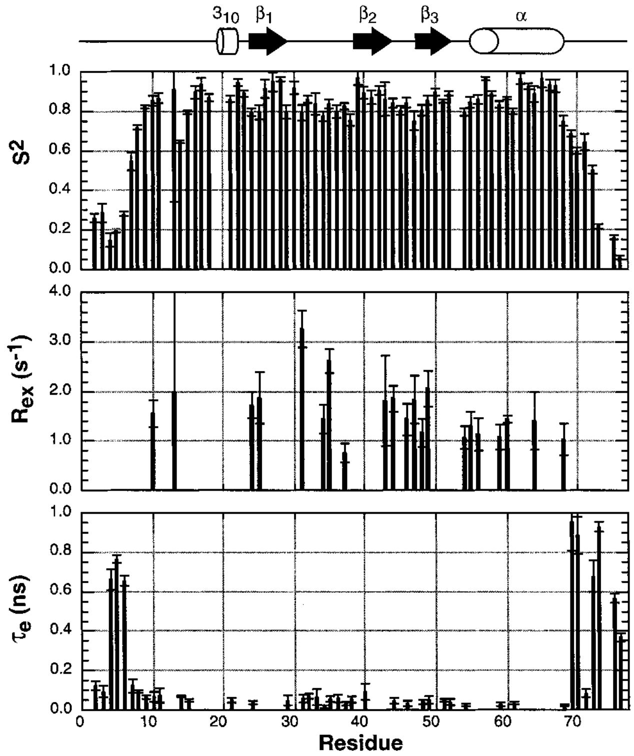

FIGURE 6: Plots of the best fit for the order parameter S^2, the conformational exchange term R_{ex}, and the internal correlation time τ_e as a function of residue number. The secondary structure of the protein is shown above the figures.

is probably also affecting Gln31, Gly35, and Phe49 which, like Ser13, exhibit large R_{ex} terms. The observed motions of the N-loop and 30's loop correlate well with regions that appear less well-ordered in the structure as seen by a comparison of Figures 4A and 6.

Titration of FRCD with a Peptide from the N-Terminus of CX$_3$CR1. Although little is known about how chemokine receptors recognize and bind their ligands, several studies have implicated the N-terminus as a specificity determining region in DARC, CCR2, CXCR1, and CXCR2 (*61*−*63*). The amino terminus also has been shown to be a domain relevant for HIV infection in CCR5, CCR2, and CXCR4 (*64*−*66*). To explore whether the N-terminus of CX$_3$CR1 is involved in binding to fractalkine, we titrated a peptide corresponding to residues 2−19 of CX$_3$CR1 into a sample of ^{15}N-labeled FRCD and monitored the effects by recording 2D ^{1}H-^{15}N HSQC spectra. Addition of the peptide resulted in a significant perturbation of the ^{1}H and ^{15}N chemical shifts of several FRCD cross-peaks as shown in Figure 7.

Since other domains of chemokine receptors have been shown to be important for ligand binding (*67*−*69*), it is not surprising that the peptide binding is weak (micromolar to millimolar) and that the complex is in fast exchange. It is interesting to note, however, that the most highly shifted cross-peaks map to distinct regions of the protein, including Thr6 through the N-loop and the 30's loop (Figure 7 and Figure 10B), regions that have been identified by mutagenesis as binding epitopes in other chemokines (Hemmerich et al., unpublished results) (*70*, *71*). These cross-peaks most likely reflect those residues which are in close proximity to or make direct contacts with the peptide. Many cross-peaks showed smaller perturbations, presumably due to indirect effects from conformational changes induced by binding of the peptide.

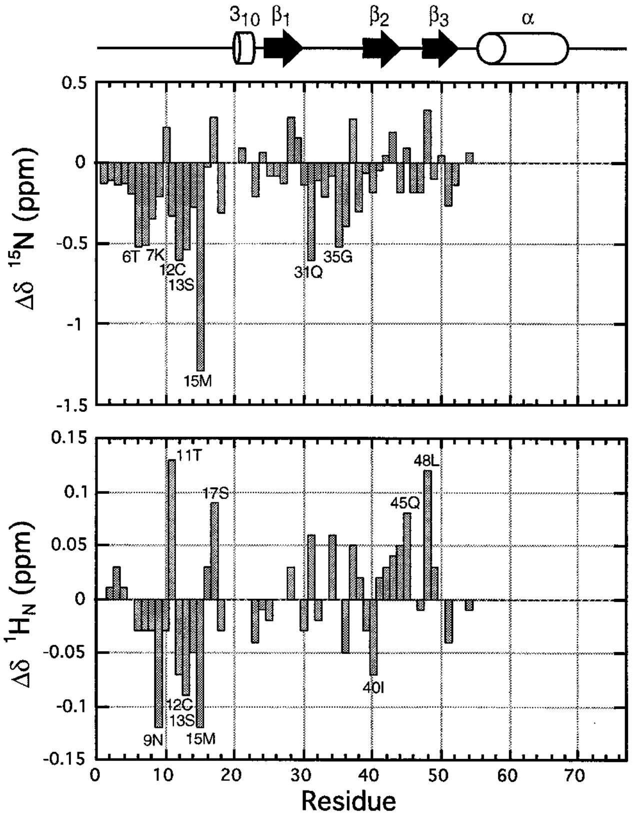

FIGURE 7: Change in ^1H_N and ^{15}N chemical shifts of FRCD upon titration with an NT peptide fragment of CX$_3$CR1. The secondary structure of the protein is shown above the figures. The ratio of peptide to FRCD is 5:1.

Importantly, residues 55−76 were unaffected by the addition of peptide, which implies that the binding is not simply due to nonspecific association. The latter observation is consistent with mutagenesis studies that show that the C-terminal regions of other chemokines are not involved in receptor binding (*72*, *73*).

DISCUSSION

FRCD is Monomeric. High-resolution structures of various CC and CXC chemokines have been reported over the last several years. All show common elements of secondary structure and similar tertiary folds. As these proteins tend to self-associate, most structures were solved as homodimers and revealed striking differences between chemokine class and mode of dimerization. In the CXC family (IL-8, MGSA/GRO), the β1 strands from two monomers assemble in an antiparallel fashion forming a six-stranded β-sheet platform topped by two helices, one from each subunit. In the CC family (MCP-1, RANTES, MIP-1β), residues near the N-terminus encompassing the first two cysteines form an unusual two-stranded antiparallel β-sheet. The net result is an elongated two-domain protein where the dimer interface is essentially a hinge between the chemokine modules, in contrast to CXC dimers which form a more compact, single domain. The present work is the first report of a structure from a third chemokine family, and we have shown that, unlike most CC and CXC chemokines, FRCD remains monomeric at high concentrations.

The fact that FRCD does not oligomerize can be rationalized on the basis of its structure and sequence. Although the sequence homology is closest to CC chemokines, the large bulge formed by the CX_3C motif (Figure 5) precludes formation of the antiparallel β-sheet at the CC dimer interface. FRCD's failure to associate as a CXC dimer is probably due to a combination of factors. In the CXC chemokine, IL-8, the dimer interface is stabilized by intersubunit hydrophobic interactions involving Leu25, Val27 (in the β1 strand), and Leu66 (in the C-terminal helix). This is also observed in MGSA/GRO where the equivalent residues are Val26, Val28, and Leu67. In FRCD, the corresponding residues are more polar (Tyr27, Gln29, Asp66), and in this sense, it resembles CC chemokines where the equivalent residues are Tyr28, Arg30, and Asp68 (in MCP-1), Tyr28, Glu30, and Glu67 (in MIP-1β), and Tyr27, Tyr29, and Glu66 (in RANTES).

The hydrophobic cluster cannot be the sole determinant of CXC-type dimerization, however, because it is present in SDF-1 (Leu26, Ile28, Leu66), yet this protein is monomeric. Other interactions that are believed to stabilize the IL-8 dimer include intersubunit electrostatic interactions between Gln59-Glu70 and Glu24-Arg26 and interactions between the end of the long C-terminal helix (56−70 in IL-8) of one subunit and the β-sheet of the other. In FRCD, these interactions are missing: Lys59-Ala70 and His26-Gln28 lack charge complementarity, and the helix is shorter (56−67) because the last 9 residues are disordered (Figures 3 and 6). Furthermore, the β1 strand, which is central to the CXC dimer interface, is shorter in FRCD than in IL-8 and GRO because of a kink caused by a hydrogen bond between the side chain NH_2 of Asn30 and the carbonyl oxygen of residues 34 and/or 36.

From a functional standpoint, the fact that FRCD is monomeric makes sense in light of the full-length protein's unusual architecture and purported role as both chemoattractant and adhesion molecule (*13*). Initially, it was postulated that chemokines bind to their receptor as dimers and that the different dimerization modes restrict the interaction of CXC chemokines to CXC receptors and CC chemokines to CC receptors (*49*). This does not appear to be the case, however, since monomeric variants of IL-8 (*74*, *75*) and MCP-1 (*52*) bind to their receptors and induce chemotaxis as effectively as the WT proteins. Although there are many possible roles for oligomerization, including those unrelated to chemotaxis, one popular hypothesis is that it may be involved in immobilizing chemokines so that a chemotactic gradient can be established (*76*). Mechanistically, this might occur through an avidity effect whereby oligomerization brings multiple heparin-binding domains together and increases the affinity of these proteins for cell surface glycosaminoglycans. If this is true, then FRCD's inability to dimerize is not surprising since the WT protein possesses a "built-in" membrane anchor and mucin-like stalk for cell surface retention and presentation. The fact that FRCD elutes from a heparin affinity column at significantly lower salt concentrations than both WT MCP-1 and a monomeric variant MCP-1P8A (see Materials and Methods) is also consistent with the idea that fractalkine does not require glycosaminoglycan presentation for function. A few other chemokines have been shown to be monomeric including SDF-1 (*77*) and MCP-3 (*78*). While these results are more difficult to rationalize in the context of a surface retention role for oligomerization, it is noteworthy that SDF-1 binds heparin more tightly than IL-8 and MCP-1 despite its monomeric nature (*79*).

Comparison to the Tertiary Structure of CC and CXC Chemokines. Structural features that distinguish FRCD from other chemokines result, in part, from the unique CX_3C pattern. On the basis of molecular models of FRCD generated with MIP-1β as a template, it was predicted that the three residue insertion in the CX_3C motif would form a helical turn in order to preserve the positions of the two disulfides relative to the other elements of secondary structure (*10*). For this reason, it also was assumed that the spacing between the first two cysteines would be restricted to zero, one, or three residues (*80*). Instead, the structure shows that the amino acids of the CX_3C motif simply bulge out, so in principle, a CX_2C chemokine could exist. It is interesting to note that the CX_3C bulge contains a consensus sequence for N-linked glycosylation (Asn-Xxx-Ser/Thr). The side chain of Asn9 is highly exposed, and although it is not yet known whether this site is glycosylated *in vivo*, N-linked glycans often occur in turns or loops such that the sugar extends out into solution (*81*).

The effect of the CX_3C bulge is to displace the C_α of the first cysteine of FRCD by 6−8 Å relative to other chemokines, even though the backbone rmsds differ by less than 2 Å (see legend of Figure 5 for further details). This causes a dramatic shift in the two regions of the protein connected by the first disulfide (the N-terminus and 30's loop) as shown by comparison to IL-8 and MCP-1 in Figure 5; the effect is magnified by the shorter 30's loop in FRCD. The bulge is held in place by hydrophobic interactions between the side chain of Ile10 in the middle of the CX_3C motif (CNITC) and Leu48 on β3 which pulls it back toward the sheet. This causes the 30's loop to move such that the β1 strand in FRCD is tilted relative to β1 in GRO and IL-8, which may also discourage CXC-type dimerization.

Additional differences between FRCD and other chemokines involve the packing of the helix against the sheet. In this region of the protein, FRCD is structurally more similar to CC chemokines than CXC chemokines. This is illustrated in Figure 8 which shows how Trp57 of FRCD packs up against Leu24, Leu41, Ala51, and Val58. In the CC chemokines MCP-1 (Figure 8A), RANTES, and MIP-1β (both not shown), the corresponding Trp packs against a similar set of residues except that a highly conserved Phe replaces Leu41 on β2. The smaller Leu side chain in FRCD allows the Trp indole to insert more deeply into the hydrophobic core compared to these chemokines. This movement is accompanied by a shift in the loop connecting β3 to the CT helix since the carboxylate of Glu55 is hydrogen-bonded to the indole HN. It also modulates the packing of residues in the N-loop (Thr16, Ser17, Lys18, Ile19) which lie above the hydrophobic core. In the CXC chemokine IL-8 (Figure 8B), the amino acid composition and packing is very different. A bulky side chain (Leu51) replaces the Ala on β3, and a residue in the N-loop (Phe17) swings in, pushing both the Trp indole and Val41 on β2 out of the core. A similar situation is seen in GRO, where the Trp is replaced by an Ile that is also displaced from the core. In GRO, the side chain of Ile63 on the helix moves in to fill the void.

Overall, a number of subtle structural and chemical features give rise to a surprisingly different molecular landscape for FRCD. This is best illustrated by GRASP (*82*)

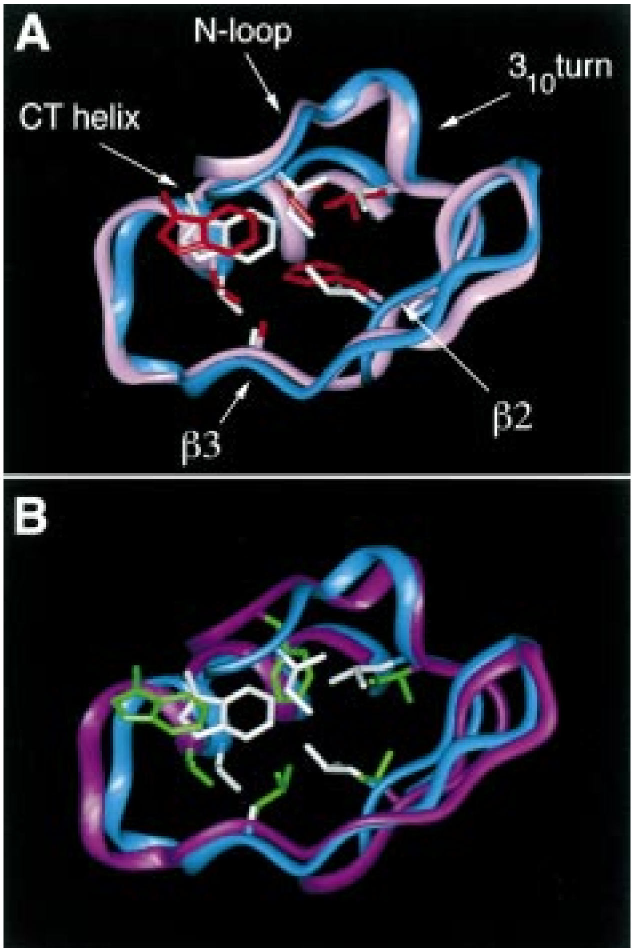

FIGURE 8: A cutaway view of FRCD (blue backbone, white side chains of Ile19, Leu24, Leu41, Ala51, Trp57, and Val58) superimposed with monomers of (A) MCP-1 (pink backbone, red side chains of Ile20, Leu25, Phe43, Ala53, Trp59, and Val60) and (B) IL-8 (purple backbone, green side chains of Phe17, Ile22, Val41, Leu51, Trp57, and Val58). The section of the N-loop that lies above the Trp has been omitted for clarity.

electrostatic potential surfaces of IL-8, MCP-1, and FRCD (Figure 9) which emphasize the variability in surface topology and charge distribution. For example, the residue immediately following the second Cys forms a large hydrophobic knob in MCP-1 and IL-8 (Tyr13 and Ile10, respectively) that is not seen in FRCD because the corresponding residue is small and polar (Ser13). Similarly, a solvent-exposed hydrophobic residue in the 3_{10} turn of FRCD and IL-8 (Leu23 and Phe21, respectively) is replaced by a basic residue in MCP-1 (Arg24), while a basic residue in the N-loop of MCP-1 and IL-8 (Arg18 and Lys15, respectively) is absent in FRCD (Ser17). Thus, although these proteins have similar folding motifs, when viewed from the perspective of the receptor, they are quite distinct.

Correlation with Mutagenesis Data. The structural differences described above are likely to be crucial for the specificity and affinity of fractalkine binding to CX_3CR1. In IL-8, MCP-1, RANTES, and several other chemokines, residues at the N-terminus of the chemokine are well-established binding determinants. However, since N-terminal peptides by themselves are ineffective, other regions must be required. In particular, residues in the 30's loop are important in IL-8 (*83*) and MCP-1 (Hemmerich et al., unpublished results) which suggests that the relative conformational differences displayed in Figure 5 are significant. N-loop residues, including many highlighted in the previous paragraph and in Figure 9, have been shown to be important in IL-8 (*73*), MCP-1 (Hemmerich et al., unpublished results), and RANTES (*71*). For example, Lowman and co-workers demonstrated that they could interchange the binding specificities of IL-8 and MGSA/GRO by exchanging N-loops (*84*). However, achieving the specificity swaps required additional mutations that affect packing interactions and control the N-loop conformation. Consequently, variations in the hydrophobic core, which supports the conformation of the

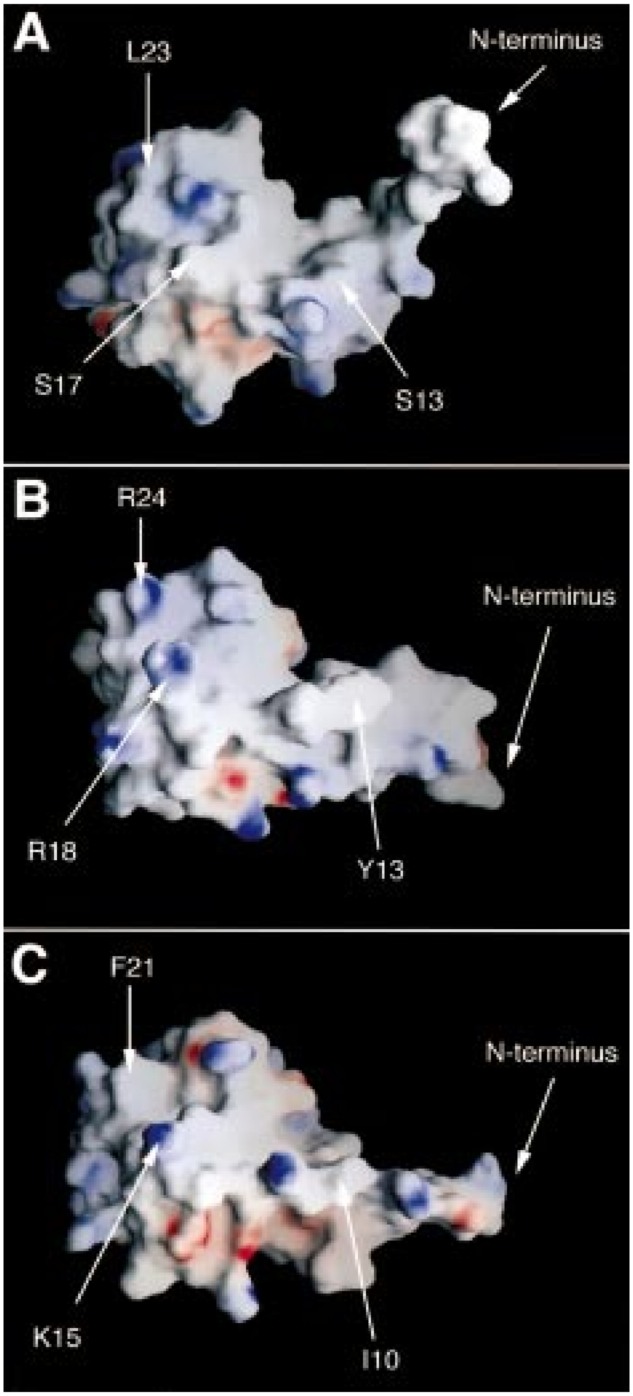

FIGURE 9: Surface electrostatic model of (A) FRCD, (B) MCP-1, and (C) IL-8. The figures were generated within the program GRASP. Electrostatic potentials were calculated within GRASP using the Poisson/Boltzmann equation and are indicated by blue for positive and red for negative.

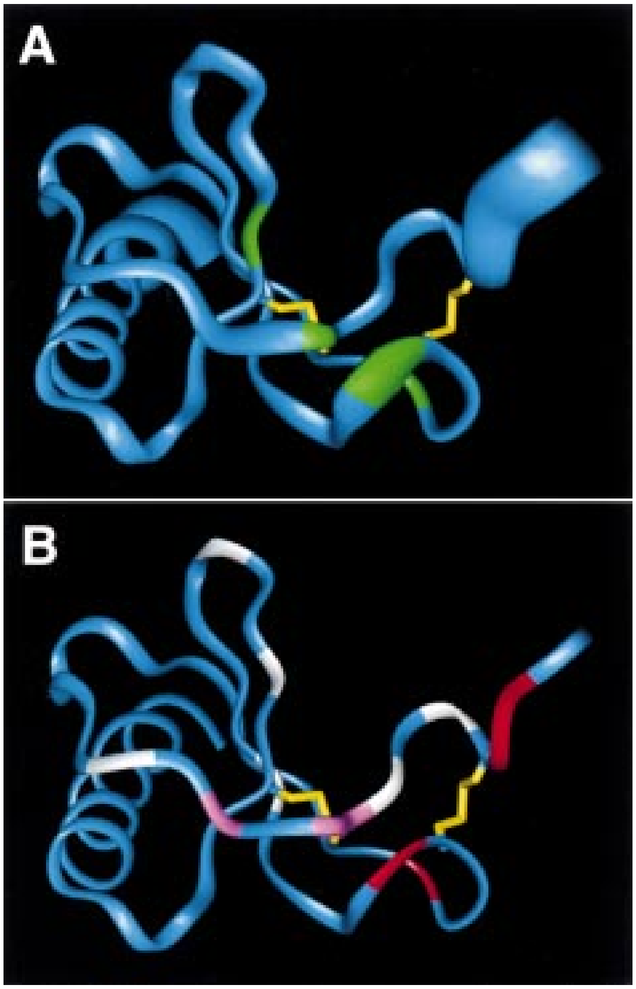

FIGURE 10: (A) Ribbon diagram of FRCD (residues 4−73) where the ribbon width is proportional to the amplitude of internal motions (1-S^2). Residues that exhibit evidence of conformational exchange ($R_{ex} \geq 2$ s^{-1}) are shown in green (Ser13, Gln31, Gly35, Phe49). (B) Ribbon diagram of FRCD (residues 4−73) highlighting residues that exhibit the largest changes in chemical shift upon peptide binding ($|\Delta\delta| > 5 \times$ digital resolution). Red indicates $|\Delta\delta^{15}\text{N}| > 0.45$ ppm (Thr6, Lys7, Gln31, Gly35); white indicates $|\Delta\delta^{1}\text{H}_\text{N}| > 0.065$ ppm (Asn9, Thr11, Ser17, Ile40, Gln45, Leu48); and pink indicates $|\Delta\delta^{15}\text{N}| > 0.45$ ppm and $|\Delta\delta^{1}\text{H}_\text{N}| > 0.065$ ppm (Cys12, Ser13, Met15). The digital resolution was 0.013 ppm for $^1\text{H}_\text{N}$ and 0.09 ppm for ^{15}N.

N-loop (Figure 8), may contribute to the binding specificity of many chemokines.

On the basis of these data, we predict that similar regions of fractalkine will be important for binding and signaling through CX$_3$CR1. This is borne out by the peptide titration data which show that residues near the N-terminus, including the CX$_3$C motif, and residues in the N-loop and 30's loop experience the largest chemical shift perturbations. We plan to use these results to guide future mutagenesis efforts and to determine at high resolution which residues of fractalkine contribute to binding both in the context of chemotaxis and adhesion.

In this regard, it will be important to determine whether the CNITC sequence is glycosylated *in vivo*. It is unclear whether glycosylation is necessary since the site is not found in the murine protein (whose CX$_3$C motif is CEIMC) (*85*). Furthermore, a synthetic, chemokine-only domain of human fractalkine effectively induced T-cell migration and blocked adhesion under static conditions (*8*). However, the synthetic material did show diminished activity for monocytes, raising the possibility that the carbohydrate moiety may contribute to chemotaxis of monocytes or adhesion under physiological blood flow conditions. Alternatively, it may be associated with other, as yet undefined roles for fractalkine.

Correlation Between Structural Variability, Dynamics, and Receptor Binding. Figure 10A shows a ribbon diagram whose width is proportional to the amplitude of motion as given by 1 − S^2. Residues which show evidence of slow conformational exchange are highlighted in green. Not surprisingly, the more dynamic regions (the N-terminus, 30's loop, and N-loop) correlate with regions that show the most structural variability between chemokines. An additional interesting finding is that the binding site for the N-terminal peptide of CX$_3$CR1 maps to roughly the same regions as seen by comparison of Figure 10, parts A and B. In particular, Ser13 and Met15, two residues which exhibit the largest chemical shift changes, show significant mobility, with Ser13 showing evidence of slow conformational exchange.

It seems reasonable that residues involved in ligand−receptor interactions would require some level of conformational flexibility to accommodate a complementary binding surface. Thus, dynamics data may be generally useful for identifying regions of proteins involved in binding (*86*, *87*). Such correlations between dynamics and binding may also help clarify the role of flexibility in protein−protein interactions and function.

ACKNOWLEDGMENT

We acknowledge and thank Michael Nilges for the ARIA extensions to X-PLOR, Wayne Boucher for providing computer enhancements to AZARA, Andy Raine and Brian Smith for X-PLOR scripts, David Fushman for advice on the dynamics calculations, and Peter Domaille for advice and assistance on all aspects of this study.

SUPPORTING INFORMATION AVAILABLE

A table containing the details of the NMR data collection and a table containing ^{1}H, ^{15}N, and ^{13}C chemical shift assignments for FRCD at pH 5.0, 22.5 °C (4 pages). Ordering information is given on any current masthead page.

REFERENCES

1. Springer, T. A. (1995) *Annu. Rev. Physiol. 57*, 827−872.
2. Salmi, M., and Jalkanen, S. (1997) *Adv. Immunol. 64*, 139−218.
3. Imhof, B. A., and Dunon, D. (1997) *Horm. Metab. Res. 29*, 614−621.
4. Crockett-Torabi, E. (1998) *J. Leukocyte Biol. 63*, 1−14.
5. Issekutz, T. B. (1993) *Curr. Top. Microbiol. Immunol. 184*, 177−185.
6. Kennedy, J., Kelner, G. S., Kleyensteuber, S., Schall, T. J., Weiss, M. C., Yssel, H., Schneider, P. V., Cocks, B. G., Bacon, K. B., and Zlotnik, A. (1995) *J. Immunol. 155*, 203−209.
7. Hedrick, J. A., Saylor, V., Figueroa, D., Mizoue, L., Xu, Y., Menon, S., Abrams, J., Handel, T., and Zlotnik, A. (1997) *J. Immunol. 158*, 1533−1540.
8. Bazan, J. F., Bacon, K. B., Hardiman, G., Wang, W., Soo, K., Rossi, D., Greaves, D. R., Zlotnik, A., and Schall, T. J. (1997) *Nature 385*, 640−644.
9. Pan, Y., Lloyd, C., Zhou, H., Dolich, S., Deeds, J., Gonzalo, J. A., Vath, J., Gosselin, M., Ma, J., Dussault, B., Woolf, E.,

Alperin, G., Culpepper, J., Gutierrez-Ramos, J. C., and Gearing, D. (1997) *Nature 387*, 611−617.

10. Wells, T. N., and Peitsch, M. C. (1997) *J. Leukocyte Biol. 61*, 545−550.
11. Witt, D. P., and Lander, A. D. (1994) *Curr. Biol. 4*, 394−400.
12. Nishiyori, A., Minami, M., Ohtani, Y., Takami, S., Yamamoto, J., Kawaguchi, N., Kume, T., Akaike, A., and Satoh, M. (1998) *FEBS Lett. 429*, 167−172.
13. Imai, T., Hieshima, K., Haskell, C., Baba, M. M. N., Nishimura, M., Kakizaki, M., Takagi, S., Nomiyama, H., Schall, T., and Yoshie, O. (1997) *Cell 91*, 521−530.
14. Raport, C. J., Schweickart, V. L., Eddy, R. L., Jr., Shows, T. B., and Gray, P. W. (1995) *Gene 163*, 295−299.
15. Reeves, J. D., McKnight, A., Potempa, S., Simmons, G., Gray, P. W., Power, C. A., Wells, T., Weiss, R. A., and Talbot, S. J. (1997) *Virology 231*, 130−134.
16. Rucker, J., Edinger, A. L., Sharron, M., Samson, M., Lee, B., Berson, J. F., Yi, Y., Margulies, B., Collman, R. G., Doranz, B. J., Parmentier, M., and Doms, R. W. (1997) *J. Virol. 71*, 8999−9007.
17. Doerring, D. S. (1992) *Functional and Structural Studies of a Small F−Actin Binding Domain*, MIT Press, Cambridge, MA.
18. Neidardt, F., Bloch, P., and Smith, D. (1974) *J. Bacteriol. 119*, 736−747.
19. Wishart, D. S., Bigam, C. G., Yao, J., Abildgaard, F., Dyson, H. J., Oldfield, E., Markley, J. L., and Sykes, B. D. (1995) *J. Biomol. NMR 6*, 135−140.
20. Wittekind, M., and Mueller, L. (1993) *J. Magn. Reson., Ser. B 101*, 201−205.
21. Grzesiek, S., and Bax, A. (1992) *J. Am. Chem. Soc. 114*, 6291−6293.
22. Clowes, R. T., Boucher, W., Hardman, C. H., Domaille, P. J., and Laue, E. D. (1993) *J. Biomol. NMR 3*, 349−354.
23. Bax, A., Clore, G. M., and Gronenborn, A. M. (1990) *J. Magn. Reson. 88*, 425−431.
24. Vuister, G. W., and Bax, A. (1992) *J. Magn. Reson. 98*, 428−435.
25. Yamazaki, T., Forman-Kay, J. D., and Kay, L. E. (1993) *J. Am. Chem. Soc. 115*, 11054−11055.
26. Talluri, S., and Wagner, G. (1996) *J. Magn. Reson., Ser. B 112*, 200−205.
27. Zuiderweg, E. R. P., McIntosh, L. P., Dahlquist, F. W., and Fesik, S. W. (1990) *J. Magn. Reson. 86*, 210−216.
28. Zuiderweg, E. R. P., Petros, A. M., Fesik, S. W., and Olejniczak, E. T. (1991) *J. Am. Chem. Soc. 113*, 370−372.
29. Clore, G. M., Kay, L. E., Bax, A., and Gronenborn, A. M. (1991) *Biochemistry 30*, 12−18.
30. Kuboniwa, H., Grzesiek, S., Delaglio, F., and Bax, A. (1994) *J. Biomol. NMR 4*, 871−878.
31. Bax, A., Max, D., and Zax, D. (1992) *J. Am. Chem. Soc. 114*, 6923−6925.
32. Vuister, G. W., Wang, A. C., and Bax, A. (1993) *J. Am. Chem. Soc. 115*, 5334−5335.
33. Archer, S. J., Ikura, M., Torchia, D. A., and Bax, A. (1991) *J. Magn. Reson. 95*, 636−641.
34. Grzesiek, S., Kuboniwa, H., Hinck, A. P., and Bax, A. (1995) *J. Am. Chem. Soc. 117*, 5312−5315.
35. Grzesiek, S., Vuister, G. W., and Bax, A. (1993) *J. Biomol. NMR 3*, 487−493.
36. Grzesiek, S., and Bax, A. (1993) *J. Am. Chem. Soc. 115*, 12593−12594.
37. Marion, D., Ikura, M., and Bax, A. (1989) *J. Magn. Reson. 84*, 425−430.
38. Kraulis, P. J., Domaille, P. J., Campbell-Burk, S. L., Vanaken, T., and Laue, E. D. (1994) *Biochemistry 33*, 3515−3531.
39. Brunger, A. T. (1992) *X-PLOR Manual*, Version 3.1, Yale University Press, New Haven, CT.
40. Nilges, M. (1995) *J. Mol. Biol. 245*, 645−660.
41. Nilges, M., Macias, M. J., O'Donoghue, S. I., and Oschkinat, H. (1997) *J. Mol. Biol. 269*, 408−422.
42. Folmer, R. H., Hilbers, C. W., Konings, R. N., and Nilges, M. (1997) *J. Biomol. NMR 9*, 245−258.
43. Barbato, G., Ikura, M., Kay, L. E., Pastor, R. W., and Bax, A. (1992) *Biochemistry 31*, 5269−5278.
44. Stonehouse, J., Clowes, R. T., Shaw, G. L., Keeler, J., and Laue, E. D. (1995) *J. Biomol. NMR 5*, 226−232.
45. Chen, H., Hughes, D. D., Chan, T. A., Sedat, J. W., and Agard, D. A. (1996) *J. Struct. Biol. 116*, 56−60.
46. Fushman, D., Cahill, S., and Cowburn, D. (1997) *J. Mol. Biol. 266*, 173−194.
47. Clore, G. M., Appella, E., Yamada, M., Matsushima, K., and Gronenborn, A. M. (1990) *Biochemistry 29*, 1689−1696.
48. Fairbrother, W. J., Reilly, D., Colby, T. J., Hesselgesser, J., and Horuk, R. (1994) *J. Mol. Biol. 242*, 252−270.
49. Lodi, P. J., Garrett, D. S., Kuszewski, J., Tsang, M. L., Weatherbee, J. A., Leonard, W. J., Gronenborn, A. M., and Clore, G. M. (1994) *Science 263*, 1762−1767.
50. Skelton, N. J., Aspiras, F., Ogez, J., and Schall, T. J. (1995) *Biochemistry 34*, 5329−5342.
51. Handel, T. M., and Domaille, P. J. (1996) *Biochemistry 35*, 6569−6584.
52. Paavola, C. D., Hemmerich, S., Grunberger, D., Polsky, I., Bloom, A., Freedman, R., Mulkins, M., Bhakta, S., McCarley, D., Wiesent, L., Wong, B., Jarnagin, K., and Handel, T. M. (1998) *J. Biol. Chem.* (in press).
53. Altieri, A. S., Hinton, D. P., and Byrd, R. A. (1995) *J. Am. Chem. Soc. 117*, 7566−7567.
54. Clubb, R. T., Ferguson, S. B., Walsh, C. T., and Wagner, G. (1994) *Biochemistry 33*, 2761−2772.
55. Metropolis, N., Rosenblum, A. W., Rosenbluth, M. N., and Teller, E. (1953) *J. Chem. Phys. 21*, 1087−1092.
56. Kraulis, P. J. (1991) *J. Appl. Crystallogr. 24*, 946−950.
57. Laskowski, R. A., Macarthur, M. W., Moss, D. S., and Thornton, J. M. (1993) *J. Appl. Crystallogr. 26*, 283−291.
58. Kay, L. E., Torchia, D. A., and Bax, A. (1989) *Biochemistry 28*, 8972−8979.
59. Luginbuhl, P., Pervushin, K. V., Iwai, H., and Wuthrich, K. (1997) *Biochemistry 36*, 7305−7312.
60. Gagne, S. M., Tsuda, S., Spyracopoulos, L., Kay, L. E., and Sykes, B. D. (1998) *J. Mol. Biol. 278*, 667−686.
61. LaRosa, G. J., Thomas, K. M., Kaufmann, M. E., Mark, R., White, M., Taylor, L., Gray, G., Witt, D., and Navarro, J. (1992) *J. Biol. Chem. 267*, 25402−25406.
62. Lu, Z. H., Wang, Z. X., Horuk, R., Hesselgesser, J., Lou, Y. C., Hadley, T. J., and Peiper, S. C. (1995) *J. Biol. Chem. 270*, 26239−26245.
63. Monteclaro, F. S., and Charo, I. F. (1996) *J. Biol. Chem. 271*, 19084−19092.
64. Frade, J. M. R., Llorente, M., Mellado, M., Alcami, J., Gutierrez-Ramos, J. C., Zaballos, A., Real, G., and Martinez, A. C. (1997) *J. Clin. Invest. 100*, 497−502.
65. Potempa, S., Picard, L., Reeves, J. D., Wilkinson, D., Weiss, R. A., and Talbot, S. J. (1997) *J. Virol. 71*, 4419−4424.
66. Rabut, G. E., Konner, J. A., Kajumo, F., Moore, J. P., and Dragic, T. (1998) *J. Virol. 72*, 3464−3468.
67. Leong, S. R., Kabakoff, R. C., and Hebert, C. A. (1994) *J. Biol. Chem. 269*, 19343−19348.
68. Samson, M., Libert, F., Doranz, B. J., Rucker, J., Liesnard, C., Farber, C. M., Saragosti, S., Lapoumeroulie, C., Cognaux, J., Forceille, C., Muyldermans, G., Verhofstede, C., Burtonboy, G., Georges, M., Imai, T., Rana, S., Yi, Y., Smyth, R. J., Collman, R. G., Doms, R. W., Vassart, G., and Parmentier, M. (1996) *Nature 382*, 722−725.
69. Tournamille, C., Le Van Kim, C., Gane, P., Blanchard, D., Proudfoot, A. E., Cartron, J. P., and Colin, Y. (1997) *J. Biol. Chem. 272*, 16274−16280.
70. Williams, G., Borkakoti, N., Bottomley, G. A., Cowan, I., Fallowfield, A. G., Jones, P. S., Kirtland, S. J., Price, G. J., and Price, L. (1996) *J. Biol. Chem. 271*, 9579−9586.
71. Pakianathan, D. R., Kuta, E. G., Artis, D. R., Skelton, N. J., and Hebert, C. A. (1997) Biochemistry 36, 9642−9648.
72. Zhang, Y. J., Rutledge, B. J., and Rollins, B. J. (1994) *J. Biol. Chem. 269*, 15918−15924.
73. Hammond, M. E., Shyamala, V., Siani, M. A., Gallegos, C. A., Feucht, P. H., Abbott, J., Lapointe, G. R., Moghadam, M.,

Khoja, H., Zakel, J., and Tekamp-Olson, P. (1996) *J. Biol. Chem. 271*, 8228−8235.

74. Rajarathnam, K., Clark-Lewis, I., and Sykes, B. D. (1995) *Biochemistry 34*, 12983−12990.
75. Lowman, H. B., Fairbrother, W. J., Slagle, P. H., Kabakoff, R., Liu, J., Shire, S., and Hebert, C. A. (1997) *Protein Sci. 6*, 598−608.
76. Tanaka, Y., Adams, D. H., and Shaw, S. (1993) *Immunol. Today 14*, 111−115.
77. Crump, M. P., Gong, J. H., Loetscher, P., Rajarathnam, K., Amara, A., Arenzana-Seisdedos, F., Virelizier, J. L., Baggiolini, M., Sykes, B. D., and Clark-Lewis, I. (1997) *Embo J. 16*, 6996−7007.
78. Kim, K. S., Rajarathnam, K., Clark-Lewis, I., and Sykes, B. D. (1996) *FEBS Lett. 395*, 277−282.
79. Bleul, C. C., Fuhlbrigge, R. C., Casasnovas, J. M., Aiuti, A., and Springer, T. A. (1996) *J. Exp. Med. 184*, 1101−1109.
80. Rollins, B. J. (1997) *Blood 90*, 909−928.
81. Imberty, A., and Perez, S. (1995) *Protein Eng. 8*, 699−709.
82. Nicholls, A., Sharp, K. A., and Honig, B. (1991) *Proteins 11*, 281−296.
83. Clark-Lewis, I., Dewald, B., Loetscher, M., Moser, B., and Baggiolini, M. (1994) *J. Biol. Chem. 269*, 16075−16081.
84. Lowman, H. B., Slagle, P. H., DeForge, L. E., Wirth, C. M., Gillece-Castro, B. L., Bourell, J. H., and Fairbrother, W. J. (1996) *J. Biol. Chem. 271*, 14344−14352.
85. Rossi, D. L., Hardiman, G., Copeland, N. G., Gilbert, D. J., Jenkins, N., Zlotnik, A., and Bazan, J. F. (1998) *Genomics 47*, 163−170.
86. Olejniczak, E. T., Zhou, M. M., and Fesik, S. W. (1997) *Biochemistry 36*, 4118−4124.
87. Kay, L. E., Muhandiram, D. R., Wolf, G., Shoelson, S. E., and Forman-Kay, J. D. (1998) *Nat. Struct. Biol. 5*, 156−163.

BI9820614